Direct Numerical Simulation of flow over a Triangular Airfoil under Martian Atmospheric Conditions

L. Caros *, O.R.H. Buxton †
Department of Aeronautics, Imperial College London, London SW7 2AZ, UK

T. Shigeta ‡, T. Nagata §, T. Nonomura ¶, K. Asai ‖
Department of Aerospace Engineering, Tohoku University Sendai, Miyagi 980-8579, JAPAN

P.E. Vincent **
Department of Aeronautics, Imperial College London, London SW7 2AZ, UK

Martian conditions present various challenges when designing rotorcraft. Specifically, the thin atmosphere and low sound speed require Martian rotor blades to operate in a low Reynolds number (1,000 to 10,000) compressible regime, for which conventional airfoils are not designed. Here we utilize PyFR to undertake high-order Direct Numerical Simulations (DNS) of flow over a triangular airfoil at a Mach number of 0.15 and Reynolds number of 3,000. Initially, span-wise periodic DNS are undertaken. Extending the domain-span-to-chord ratio from 0.3 to 0.6 leads to better agreement with wind tunnel data at higher angles of attack, when the flow is separated. This is because smaller domain spans artificially suppress three-dimensional breakdown of coherent structures above the suction surface of the airfoil. Subsequently, full-span DNS in a virtual wind tunnel are undertaken, including all wind tunnel walls. These capture blockage and wall boundary layer effects, leading to better agreement with wind tunnel data for all angles of attack compared to span-wise periodic DNS. The results are important in terms of understanding discrepancies between previous span-wise periodic DNS and wind tunnel data. They also demonstrate the utility of high-order DNS as a tool for accurately resolving flow over triangular airfoils under Martian conditions.

*Doctoral Candidate, Department of Aeronautics, Imperial College London, London SW7 2AZ, UK, lidia.caros-roca19@imperial.ac.uk.

†Reader, Department of Aeronautics, Imperial College London, London SW7 2AZ, UK, o.buxton@imperial.ac.uk.

‡Master's course student, Department of Aerospace Engineering, Tohoku University Sendai, Miyagi 980-8579, JAPAN, tsuyoshi.shigeta.t7@dc.tohoku.ac.jp.

§Assistant Professor, Department of Aerospace Engineering, Tohoku University Sendai, Miyagi 980-8579, JAPAN, nagata@aero.mech.tohoku.ac.jp.

¶Associate Professor, Department of Aerospace Engineering, Tohoku University Sendai, Miyagi 980-8579, JAPAN, nonomura@aero.mech.tohoku.ac.jp.

‖Professor, Department of Aerospace Engineering, Tohoku University Sendai, Miyagi 980-8579, JAPAN, keisuke.asai.c3@tohoku.ac.jp, Associate Fellow.

**Professor, Department of Aeronautics, Imperial College London, London SW7 2AZ, UK, p.vincent@imperial.ac.uk.

I. Introduction

On April 19 2021, NASA's Ingenuity Helicopter undertook the first ever heavier-than-air flight on Mars [1]. Ingenuity has a total mass of 1.8 kg and features two counterrotating hingeless rotors with a diameter of 1.21 m, each comprising two blades based on conventional airfoil profiles [2].

Martian atmospheric conditions are very different to those on Earth, and present various challenges when designing rotorcraft. Specifically, Mars has a thin atmosphere with a very low surface density (≈ 0.017 kg/m^3) and pressure (≈ 0.75975 kPa) compared to Earth, reducing rotor lift and efficiency. Additionally, the speed of sound on Mars is approximately 72% of that on Earth due to its low surface temperature (average of -63 °C) and atmospheric composition (95% carbon dioxide), which puts a limit on rotor speeds in order to avoid high Mach numbers at the blade tip. Taken together, these conditions require Martian rotor blades to operate in a low Reynolds number ($1,000$ to $10,000$) compressible flow regime; for which conventional airfoils have not been designed, and optimal airfoils have yet to be developed.

Previous experimental studies of flow over airfoils under Martian atmospheric conditions have investigated the performance of conventional (NACA0012) airfoils [3–5] and non-conventional airfoils such as insect (dragonfly) inspired airfoils [6, 7], angular airfoils [8], triangular airfoils [9, 10], and thin flat and cambered plates [4, 5]. Non-conventional airfoils have been shown to give a higher aerodynamic performance at low-Reynolds numbers [7] than conventional airfoils. Previous Computational Fluid Dynamics (CFD) studies, of which there have been relatively few, include Reynolds Averaged Navier-Stokes (RANS) simulations [11] and Direct Numerical Simulations (DNS) [9] of flow over a triangular airfoil at various angles of attack. Certain RANS results [11] were found to achieve good agreement with available experimental data; although the degree of agreement was sensitive to the closure that was employed, with the recent WA model [12] performing the best. DNS results [9] were found to qualitatively capture experimentally observed non-linearity in the lift curve. However, quantitative differences remained, particularly at high angles of attack. Our hypothesis is that these resulted from the relatively small domain span to chord ratio that was employed and/or the absence of wind tunnel walls in the simulations.

In the present work we utilise PyFR [13] to undertake high-order accurate DNS of flow over the triangular airfoil studied both experimentally and computationally by Munday et al. [9]. Specifically, span-wise periodic DNS are undertaken with various domain spans, as well as full-span DNS in a virtual wind tunnel including all wind tunnel walls, for a range of angles of attack, with a fixed free-stream Mach number $M = 0.15$ and a chord based Reynolds number $Re = 3,000$. Results are compared with both the experimental and computational data of Munday et al. [9] and used to assess the effect of both domain span and wind tunnel walls on DNS accuracy.

Sec. II presents the methodology for the current work. Next, Sec. III investigates the effect of domain span. Sec. IV describes the effects of wind tunnel walls. Finally, the conclusions and future work are presented in Sec. V.

II. Methodology

A. Test Case

The experimental studies of Munday et al. [9] were carried out in the Mars Wind Tunnel (MWT) at Tohoku University [14]. The test section of the MWT measures 400 mm in length, 150 mm in height, and 100 mm in width; with the top and bottom walls of the test section inclined at 1.3 degrees to compensate for boundary layer growth. The triangular airfoil was placed in the middle of the test section. It had a chord of 30 mm, a maximum thickness of 1.5 mm at 9 mm from the leading edge, and spanned the width of the wind-tunnel test section; with a span to chord ratio of 3.33. Various quantities were measured, including time-averaged lift, drag and pressure coefficients defined as

$$C_L = \frac{F_L}{q_\infty A}\,, \qquad C_D = \frac{F_D}{q_\infty A}\,, \qquad C_P = \frac{p - p_a}{q_\infty}\,, \tag{1}$$

respectively, where F_L and F_D are the time-averaged lift and drag forces, respectively, measured with a force balance, p is the time-averaged static pressure obtained via mid-span pressure tappings and pressure-sensitive paint (PSP), p_a is a time-averaged reference static pressure measured at the airfoil apex, A is the airfoil planform area, and q_∞ is the time-averaged dynamic pressure. The time-averaged dynamic pressure was obtained via

$$q_\infty = p_{Ts} - p_e, \tag{2}$$

where p_{Ts} is the time-averaged total pressure measured with a pitot tube in the settling chamber of the wind tunnel and p_e is the time-averaged static pressure measured at the entrance of the test section.

The computational studies of Munday et al. [9] comprised span-wise periodic DNS, with a domain-span to chord ratio of 0.3.

Both the experimental and computational studies of Munday et al. [9] were undertaken with $M = 0.15$ and $M = 0.5$, and $Re = 3,000$ and $Re = 10,000$, for various angles of attack α in the range $0^\circ \leq \alpha \leq 15^\circ$. In the present work we focus on the case with $M = 0.15$ and $Re = 3,000$. Under these conditions the triangular airfoil has a highly nonlinear lift curve, and various flow regimes can be identified, including a laminar two-dimensional regime when $\alpha < 7^\circ$ and a turbulent three-dimensional regime when $\alpha > 9^\circ$. Specifically, when $\alpha < 7^\circ$ flow separation and subsequent vortex roll-up happens at the apex of the triangular airfoil. However, when $\alpha > 9^\circ$, flow separates at the leading edge, with larger and stronger vortices rolling up on the suction surface of the airfoil compared to those shed from the apex. These more energetic vortices induce a large area of low pressure on the suction surface, which enhances lift. In the transition region between these two regimes separation migrates from the apex to the leading edge, resulting in rapid variation of lift with α. In the experimental studies of Munday et al. [9] this transition occurs in the region $\alpha = 8^\circ - 9^\circ$. However, in the computational studies of Munday et al. [9] it occurs in the region $\alpha = 7^\circ - 8^\circ$.

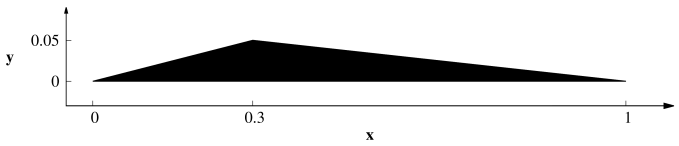


Fig. 1 Schematic of triangular airfoil profile.

B. Governing Equations

In the present work we used PyFR [13] to solve the compressible Navier-Stokes equations for an ideal gas with constant viscosity. These can be written as

$$\frac{\partial \mathbf{u}}{\partial t} + \boldsymbol{\nabla} \cdot \mathbf{f} = 0, \tag{3}$$

where $\mathbf{u} = \mathbf{u}(\mathbf{x}, t) = (\rho, \rho v_x, \rho v_y, \rho v_z, E)$ is the solution with ρ the fluid density, $\mathbf{v} = (v_x, v_y, v_z)$ the fluid velocity and E the total energy per unit volume, and where $\mathbf{f} = \mathbf{f}(\mathbf{u}, \boldsymbol{\nabla}\mathbf{u}) = \mathbf{f^i} - \mathbf{f^v}$ is the flux, with $\mathbf{f^i}$ the inviscid flux given by

$$\mathbf{f^i} = \begin{Bmatrix} \rho v_x & \rho v_y & \rho v_z \\ \rho v_x^2 + p & \rho v_y v_x & \rho v_z v_x \\ \rho v_x v_y & \rho v_y^2 + p & \rho v_z v_y \\ \rho v_x v_z & \rho v_y v_z & \rho v_z^2 + p \\ v_x(E+p) & v_y(E+p) & v_z(E+p) \end{Bmatrix}, \tag{4}$$

where p is the pressure, which for an ideal gas is given by

$$p = (\gamma - 1)\left(E - \frac{1}{2}\rho \|\mathbf{v}\|^2\right), \tag{5}$$

with $\gamma = c_p/c_v$, where c_p and c_v are specific heat capacities at constant pressure and volume, respectively, and $\mathbf{f^v}$ is the viscous flux given by

$$\mathbf{f^v} = \begin{Bmatrix} 0 & 0 & 0 \\ \mathscr{T}_{xx} & \mathscr{T}_{yx} & \mathscr{T}_{zx} \\ \mathscr{T}_{xy} & \mathscr{T}_{yy} & \mathscr{T}_{zy} \\ \mathscr{T}_{xz} & \mathscr{T}_{yz} & \mathscr{T}_{zz} \\ v_i \mathscr{T}_{ix} + \Delta \partial_x T & v_i \mathscr{T}_{iy} + \Delta \partial_y T & v_i \mathscr{T}_{iz} + \Delta \partial_z T \end{Bmatrix}, \tag{6}$$

where the stress-energy tensor is given by

$$\mathscr{T}_{ij} = \mu(\partial_i v_j + \partial_j v_i) - \frac{2}{3}\mu\delta_{ij}\boldsymbol{\nabla}\cdot\mathbf{v}, \tag{7}$$

with μ the dynamic viscosity, $\Delta = \mu c_p/Pr$, with Pr the Prandtl number, and T is the temperature, which for an ideal gas is given by

$$T = \frac{1}{c_v}\frac{1}{\gamma - 1}\frac{p}{\rho}. \tag{8}$$

In the current study values of $\gamma = 1.4$ and $Pr = 0.71$ were employed.

C. Solver and Numerical Method

PyFR is based on the high-order Flux Reconstruction approach of Huynh [15]. In the present work fourth-order polynomials were used to represent the solution within each element of the mesh, thus nominally achieving fifth-order accuracy in space. A Rusanov Riemann solver was used to calculate the inter-element inviscid fluxes, the Local Discontinuous Galerkin approach was used to calculate the inter-element viscous fluxes, an explicit RK45 scheme [16] was employed to advance the solution in time, no anti-aliasing was employed, and all runs were performed using double precision arithmetic.

Simulations were undertaken using Nvidia Tesla V100-SXM2-16GB GPUs on Cirrus at the EPCC Advanced Computing Facility and Nvidia Tesla P100-16GB GPUs on Piz Daint at the Swiss National Supercomputing Centre (CSCS).

III. Effect of domain span

A. Overview

In this section the effect of domain span on the accuracy of span-wise periodic DNS is investigated. Specifically, results from two-dimensional PyFR simulations, and results from span-wise periodic PyFR simulations with domain span to chord ratios of 0.3, 0.6 and 0.9, are compared with previous experimental and computational results from Munday et al. [9]. All simulations were undertaken using PyFR v1.10.0.

B. Setup

1. Computational domain

A schematic of the triangular airfoil profile is shown in Fig. 1. It is defined to have a chord of 1.0 and a maximum thickness of 0.05 at a distance of 0.3 from the leading edge. The origin in the streamwise-vertical xy-plane is located at the leading edge of the airfoil when $\alpha = 0°$. When changing the angle of attack, the airfoil is rotated about its trailing edge. The dimensions of the computational domain are $x \in [-10, 20]$ in the streamwise direction and $y \in [-10, 10]$ in

the vertical direction. These are the same as those used in the computational study of Munday et al. [9]. The span-wise extent of the domain is varied, from zero for the two-dimensional cases to $z \in [0, \delta_z]$ for the three-dimensional cases, where the domain span δ_z is 0.3, 0.6 and 0.9.

2. Meshes

For two-dimensional cases meshes are comprised of structured and unstructured regions in the streamwise-vertical xy-plane. Specifically, structured quadrilateral meshes are located adjacent to the airfoil surfaces, extending a distance of 0.2 normally from the upper surface and 0.1 normally from the lower surface into the domain. For high angles of attack structured regions on the upper surface are augmented after the apex to extend a distance 0.5 normally into the domain. Structured quadrilateral meshes are also located in the wake region, extending a distance of 6.0 downstream of the airfoil. The remainder of the streamwise-vertical xy-plane meshes are tessellated with an unstructured mix of quadrilaterals and triangles. Figure 2 shows the mesh in the streamwise-vertical xy-plane for $\alpha = 12°$. The two-dimensional meshes have $\sim 18 \times 10^3$ elements, and $\sim 412 \times 10^3$ degrees of freedom per equation in total when fourth-order solution polynomials are used to represent the solution with each element.

For three-dimensional cases the analogous two-dimensional mesh is extruded in the span-wise z direction, generating hexahedra and triangular prisms throughout the domain. The largest three-dimensional meshes have $\sim 155 \times 10^3$ elements, and $\sim 19.4 \times 10^6$ degrees of freedom per equation in total when fourth-order solution polynomials are used to represent the solution with each element.

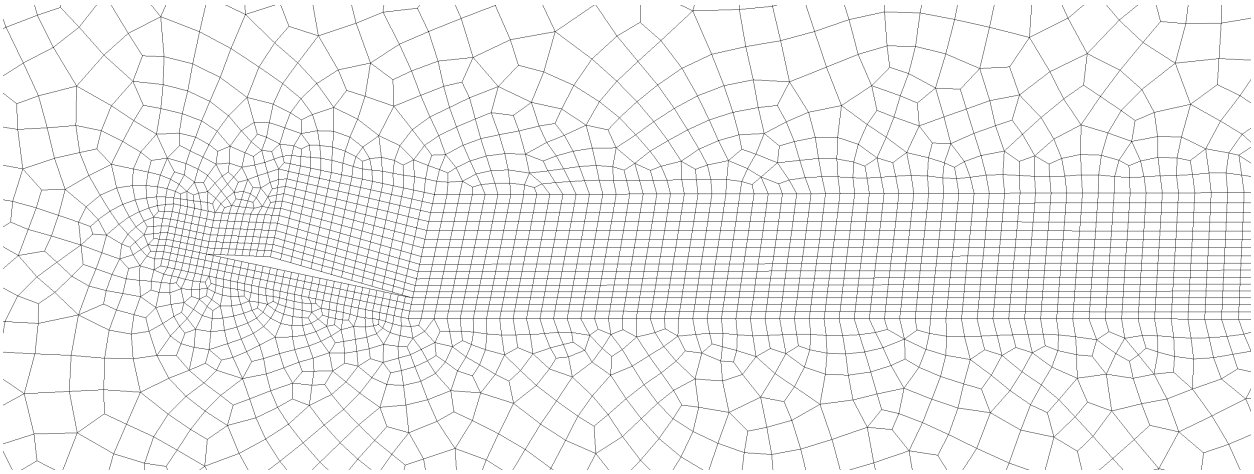


Fig. 2 Zoomed in view of mesh in the streamwise-vertical xy-plane used for 2D and span-wise periodic DNS with $\alpha = 12°$.

3. Boundary Conditions

At the $x = -10$ inflow, $x = 20$ outflow, $y = -10$ bottom, and $y = 10$ top planes a characteristic boundary condition was applied. Specifically, a density $\rho = 1.0$, velocity $\mathbf{v} = \{v_x, v_y, v_z\} = \{1.0, 0.0, 0.0\}$ and pressure $p = 31.746$

were prescribed. An impermeable no-slip adiabatic boundary condition was prescribed at the airfoil surface. For the three-dimensional cases periodic boundary conditions were applied in the span-wise direction. Taken together these conditions achieved $M = 0.15$ and $Re = 3,000$. Note that no turbulence was injected at the inflow.

4. Startup process and data extraction

All simulations were initiated at $t = 0$ with a uniform density $\rho = 1.0$, velocity $\mathbf{v} = \{v_x, v_y, v_z\} = \{1.0, 0.0, 0.0\}$ and pressure $p = 31.746$ throughout the entire domain. Simulations were advanced a period t_t to remove initial transients and then for a further t_e, henceforth referred to as the Data Extraction Period during which data was extracted for analysis. For two-dimensional simulations $t_t = 10t_c$, $t_e = 10t_c$ when $\alpha < 8$, and $t_t = 15t_c$, $t_e = 15t_c$ when $\alpha \geq 8$, and for three-dimensional simulations $t_t = 40t_c$, $t_e = 20t_c$ when $\alpha < 8$, and $t_t = 100t_c$, $t_e = 50t_c$ when $\alpha \geq 8$, and with in all cases $t_c = c/u_\infty$ where u_∞ is the x-velocity magnitude measured at the center of the $x = -10$ inflow plane time-averaged over the Data Extraction Period.

Note that for the first $5t_c$ of each three-dimensional simulation the velocity prescribed at the $x = -10$ inflow plane was modified to have a time-dependent component as follows $\mathbf{v} = \{1 + 0.2\sin(100t), 0.2\sin(100t), 0.2\sin(100t)\}$ in order to trigger flow instabilities.

C. Results

Figure 3 shows plots of C_L and C_D as a function of α for the 2D and span-wise periodic DNS undertaken with PyFR, as well as for the previous DNS and experimental studies of Munday et al.[9]. For the PyFR simulations C_L and C_D were obtained using Eq. (1), where F_L and F_D were obtained by time-averaging the sum of viscous and pressure forces on the airfoil in the y and x directions, respectively, over the Data Extraction Period, and q_∞ was obtained via

$$q_\infty = \frac{1}{2}\rho_\infty u_\infty^2 \tag{9}$$

where ρ_∞ and u_∞ are the density and velocity magnitude, respectively, measured at the center of the $x = -10$ inflow plane time-averaged over the Data Extraction Period.

The 2D PyFR results are seen to be in reasonable agreement with the experimental C_L and good agreement with the experimental C_D for low α. However, as α increases and the flow becomes highly-separated and unsteady, the 2D PyFR simulations start to significantly over-predict both C_L and C_D relative to the experimental results, with discrepancies in C_L reaching 80% when $\alpha = 15°$.

The span-wise periodic DNS results obtained using PyFR with $\delta_z = 0.3$ are seen to be in excellent agreement with both C_L and C_D obtained from the previous DNS of Munday et al. [9], which were undertaken using the same domain span to chord ratio of 0.3. The trends in both C_L and C_D are also closer to the experimental data than the 2D PyFR

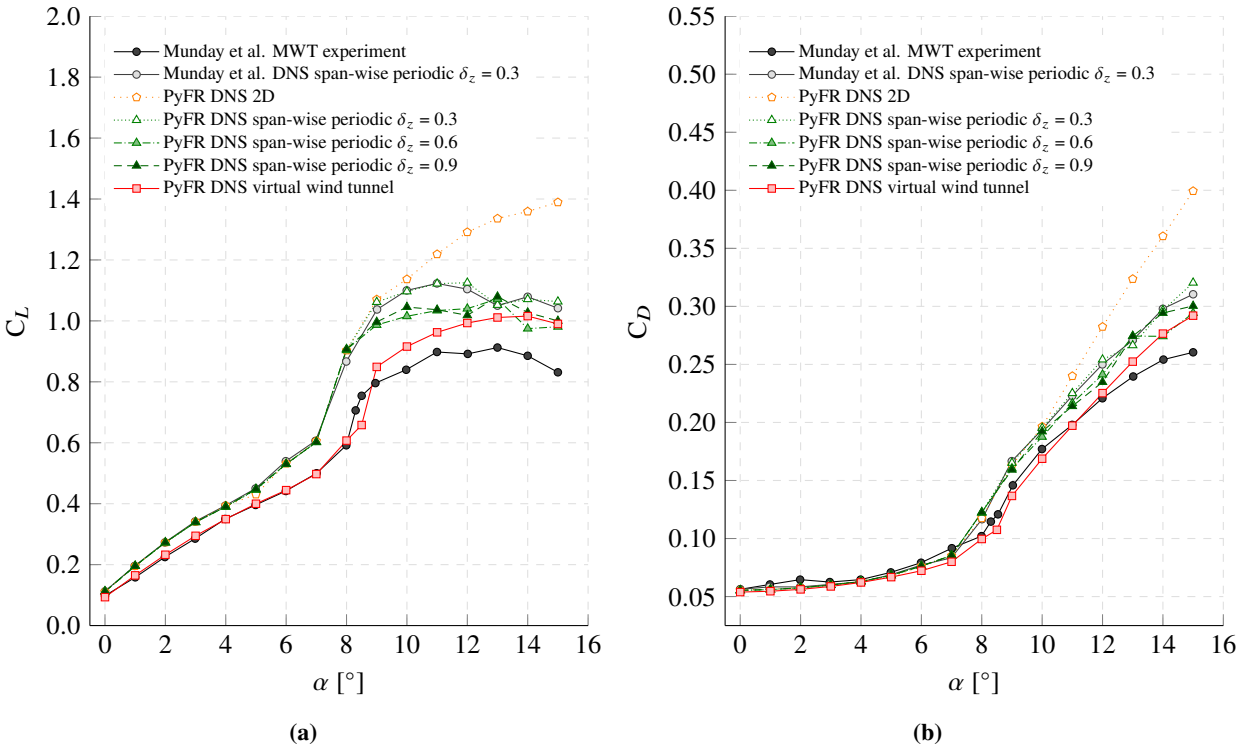


Fig. 3 Plots of lift coefficient C_L (a) and drag coefficient C_D (b) as a function of angle of attack α obtained from the MWT experiments of Munday et al. [9], span-wise periodic DNS with δ_z = 0.3 of Munday et al. [9], 2D DNS using PyFR, span-wise periodic DNS with δ_z = 0.3, δ_z = 0.6, δ_z = 0.9 using PyFR, and DNS in a virtual wind tunnel using PyFR.

results. This is because the span-wise periodic DNS can capture breakdown of large vortical structures shed above the suction surface of the airfoil. The importance of this effect becomes particularly apparent when $\alpha \geq 9°$, after the separation point has moved to the leading edge of the airfoil.

The span-wise periodic DNS results obtained using PyFR with $\delta_z = 0.6$ and $\delta_z = 0.9$ are similar to those obtained with $\delta_z = 0.3$ when $\alpha \leq 9°$. However, when $\alpha \geq 9°$ they achieve better agreement with the experimental C_L and C_D. Specifically, except for when $\alpha = 13°$, discrepancies relative to the experimental C_L and C_D are reduced by between 20% and 50%. However, we note that changing from $\delta_z = 0.6$ to $\delta_z = 0.9$ has little additional effect on both C_L and C_D.

Figure 4 shows plots of C_P for $\alpha = 6°$ and $\alpha = 12°$ on the suction surface of the airfoil as a function of $\tilde{x} = x/a$, where a is the x-wise distance between the leading and trailing edge of the airfoil, for the 2D and span-wise periodic DNS undertaken with PyFR, as well as for the previous DNS and experimental studies of Munday et al.[9]. For the span-wise periodic DNS C_P was obtained using Eq. (1), where p was obtained at each $\tilde{x}$ by space-time-averaging static pressure on the suction surface of the airfoil in span and over the Data Extraction Period, p_a was obtained by space-time-averaging static pressure within all mesh cells that had vertices coincident with the apex of the airfoil and over the Data Extraction Period, and q_∞ was obtained via Eq. (9), where ρ_∞ is the density measured at the center of the

$x = -10$ inflow plane time-averaged over the Data Extraction Period.

When $\alpha = 6^\circ$ the 2D and span-wise periodic DNS results obtained using PyFR are seen to be in good agreement with C_P obtained from the previous DNS and experiments of Munday et al. [9]. However, when $\alpha = 12^\circ$ differences occur. Specifically, the 2D PyFR simulations start to significantly over-predict C_P above the down-stream section of the airfoil relative to the experimental results. Span-wise periodic DNS results obtained using PyFR with $\delta_z = 0.3$ are seen to reduce this discrepancy, and achieve good agreement with C_P distributions obtained from the previous DNS of Munday et al. [9], which were undertaken using the same domain span to chord ratio of 0.3. Increasing the domain span to $\delta_z = 0.6$ is seen to reduce the discrepancy further still, dramatically flattening the C_P distribution above the down-stream section of the airfoil, and bringing it significantly closer to the experimental results. However, further increasing the domain span from $\delta_z = 0.6$ to $\delta_z = 0.9$ has little additional effect on C_P.

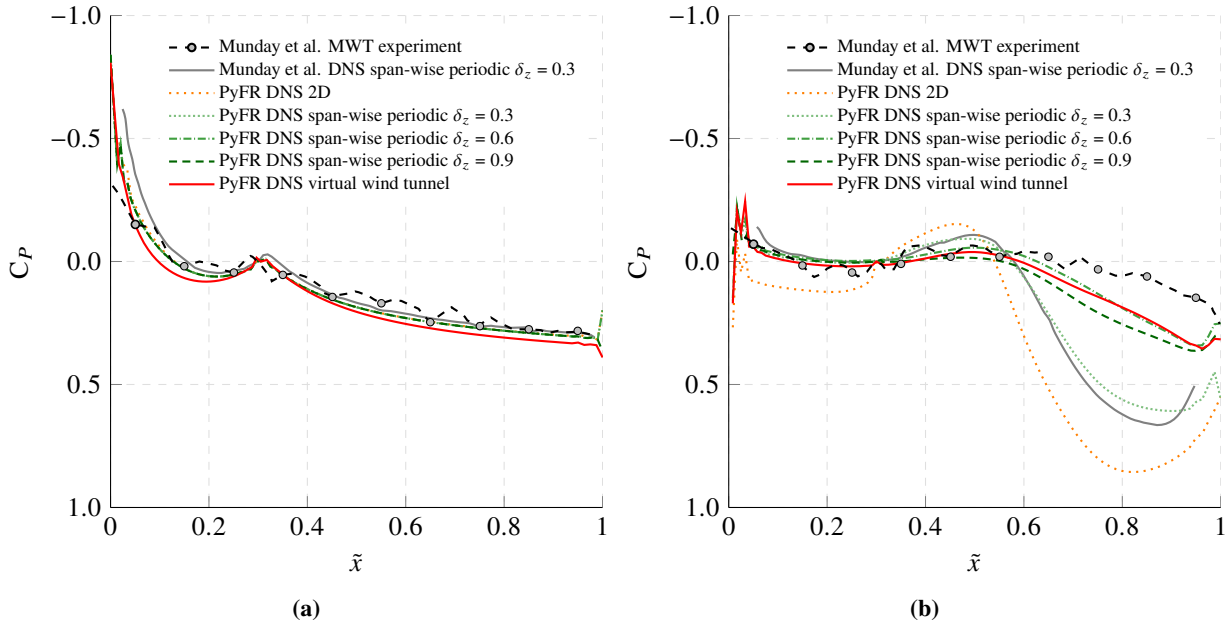


Fig. 4 Plots of pressure coefficient C_P as a function of $\tilde{x}$ for angles of attack $\alpha = 6^\circ$ (a) and $\alpha = 12^\circ$ (b) on the suction surface of the airfoil obtained from the MWT experiments of Munday et al. [9], span-wise periodic DNS with $\delta_z = 0.3$ of Munday et al. [9], 2D DNS using PyFR, span-wise periodic DNS with $\delta_z = 0.3$, $\delta_z = 0.6$, $\delta_z = 0.9$ using PyFR, and DNS in a virtual wind tunnel using PyFR.

Figure 5 shows instantaneous Q-criterion iso-surfaces, coloured by velocity magnitude, for the case with $\alpha = 12^\circ$ when $\delta_z = 0.3$ and $\delta_z = 0.9$, and at different points in the shedding cycle. Specifically, the left-hand column shows the instant of maximum lift in a specific shedding cycle, the middle column shows an instant of intermediate lift in the same cycle, and the right-hand column shows the instant of minimum lift in the same cycle. Figure 6 shows instantaneous density gradient, at the instant of maximum lift in a specific shedding cycle, for the case with $\alpha = 12^\circ$ when $\delta_z = 0.3$ and $\delta_z = 0.9$, and in different y-z planes. Specifically, the left-hand column shows a plane at the trailing edge, the middle column shows a plane half a chord downstream from the trailing edge, and the right-hand column shows a plane

one chord downstream from the trailing edge. Note that for the case with $\delta_z = 0.3$ the periodic data is repeated three times to facilitate comparison with the $\delta_z = 0.9$ case.

Taken together, Figures 5 and 6 show how using $\delta_z = 0.3$ imposes non-physical periodicity, and artificially suppresses the three-dimensional breakdown of coherent structures that form above the suction surface of the airfoil and in the wake.

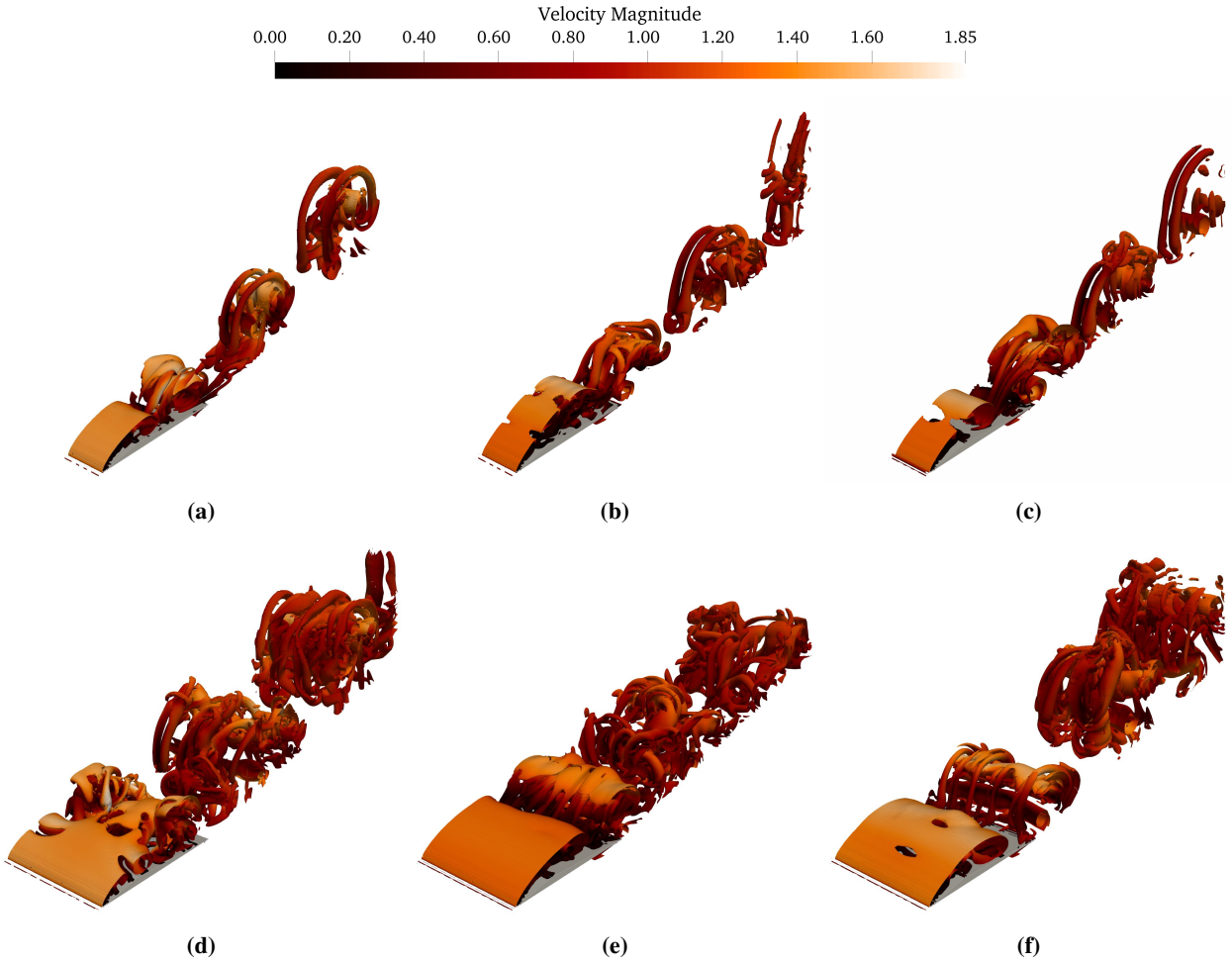


Fig. 5 Images of instantaneous Q-criterion isosurfaces Q = 1, coloured by velocity magnitude, for $\alpha = 12°$ when $\delta_z = 0.3$ (a), (b) and (c), and $\delta_z = 0.9$ (d), (e) and (f), at different points in the shedding cycle: maximum lift (a) and (d), intermediate lift (b) and (e), and minimum lift (c) and (f).

IV. Effect of wind tunnel walls

A. Overview

In this section the effect of wind tunnel walls on the accuracy of DNS is investigated. Specifically, results from full-span DNS of the triangular airfoil in a virtual wind tunnel, including all wind tunnel walls, are compared with previous experimental and computational results from Munday et al. [9]. All simulations were undertaken using PyFR v1.10.0.

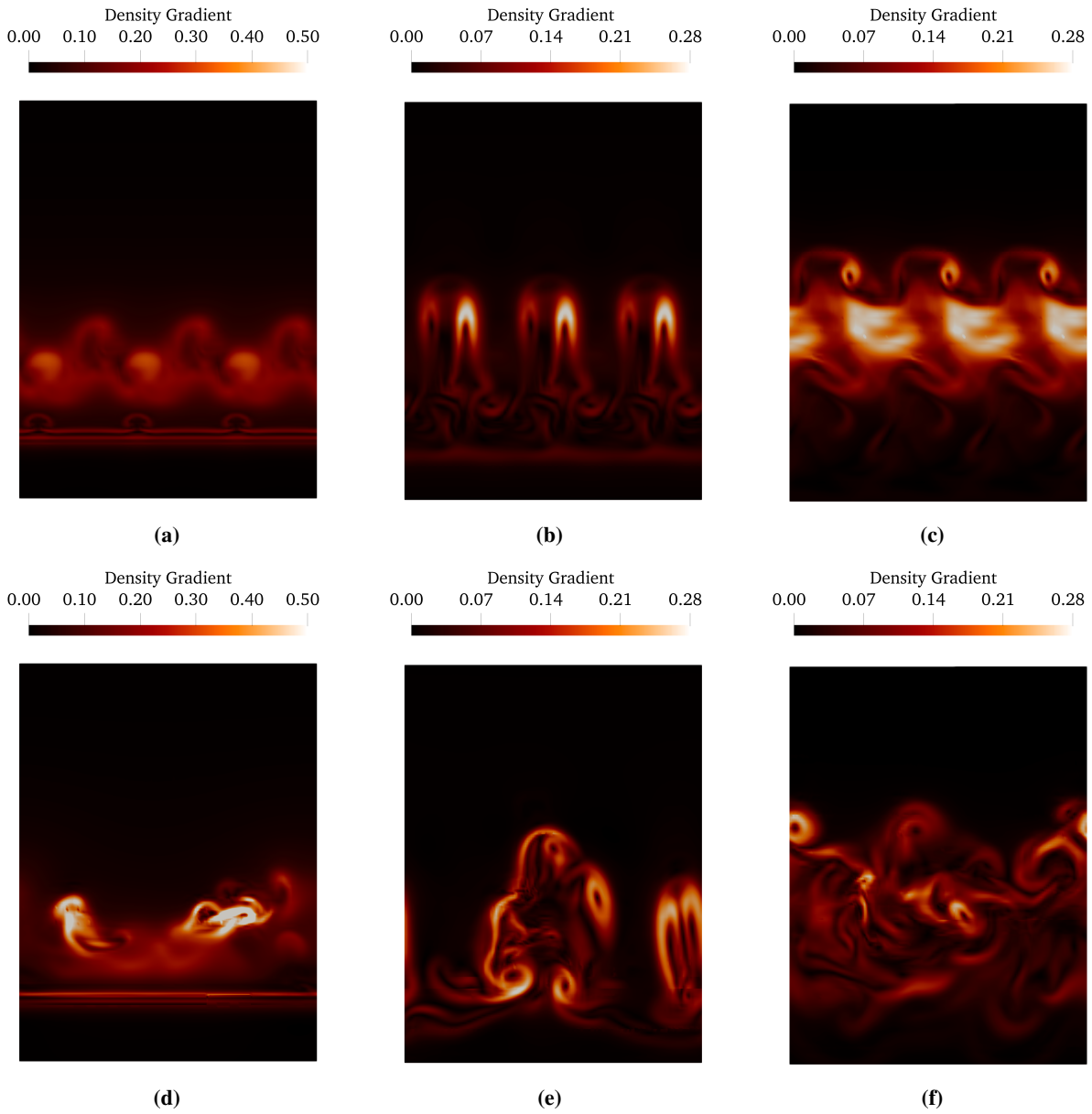


Fig. 6 Images of instantaneous density gradient, at the instant of maximum lift in a specific shedding cycle, for $\alpha = 12°$ when $\delta_z = 0.3$ (a), (b) and (c), and $\delta_z = 0.9$ (d), (e) and (f), in different y-z planes: (a) and (d) show a plane at the trailing edge, (b) and (e) show a plane half a chord downstream from the trailing edge, and (c) and (f) show a plane one chord downstream from the training edge. Note that for the case with $\delta_z = 0.3$ the periodic data is repeated three times to facilitate comparison with the $\delta_z = 0.9$ case.

B. Setup

1. Computational domain

As per Sec. III.B.1, the triangular airfoil is defined to have a chord of 1.0 and a maximum thickness of 0.05 at 0.3 from the leading edge. The origin in the streamwise-vertical xy-plane is located at the leading edge of the airfoil when $\alpha = 0°$. When changing the angle of attack, the airfoil is rotated about its trailing edge. The dimensions of the

computational domain are $x \in [-5, 8.333]$ in the streamwise direction, $y \in [-2.5, 2.5]$ in the vertical direction at the inlet, and $z \in [0, 3.333]$ in the span-wise direction, with the top and bottom walls inclined at an angle of 1.3° to the streamwise direction. This configuration matches the working section of the Tohoku Mars Wind Tunnel, in which the experiments of Munday et al. [9] were undertaken.

2. Meshes

Meshes are constructed by extruding 2D streamwise-vertical xy-plane meshes in the span-wise z direction. The streamwise-vertical xy-plane meshes are comprised of structured and unstructured regions. Specifically, structured quadrilateral meshes are located adjacent to the airfoil surfaces, extending a distance of 0.2 normally from the upper surface and 0.1 normally from the lower surface into the domain. For high angles of attack structured regions on the upper surface are augmented after the apex to extend a distance 0.5 normally into the domain. Structured quadrilateral meshes are also located in the wake region, extending a distance of 6.0 downstream of the airfoil, and adjacent to the top and bottom walls, extending a distance of 0.3 normally into the domain. The remainder of the streamwise-vertical xy-plane meshes are tessellated with an unstructured mix of quadrilaterals and triangles. Extrusion of the 2D meshes in the span-wise z direction, generates hexahedra and triangular prisms throughout the domain.

Mesh density is selected to achieve DNS resolution throughout the domain. Specifically, mesh cells adjacent to the wind tunnel walls are sized such that $\delta_\nu > \Delta$ everywhere, where δ_ν is the local diffusive length scale of a Blasius boundary layer solution and

$$\Delta = \frac{\sqrt[3]{V}}{p+1} \tag{10}$$

is an estimate of the local solution point spacing, with V the local element volume and p the polynomial order used to represent the solution within each element of the mesh. Additionally, in the wake we a posteriori verify in Appendix A that $2.5\eta > \Delta$ everywhere, where

$$\eta = \left(\frac{\nu^3}{\varepsilon}\right)^{1/4} \tag{11}$$

is the Kolmogorov length scale, with ν the kinematic viscosity and

$$\varepsilon = 2\nu S_{ij} S_{ij} \tag{12}$$

the dissipation rate, where S_{ij} is the fluctuating rate-of-strain tensor. This is within the threshold required to achieve DNS resolution given the simulations are nominally fifth-order accurate in space [17].

Figure 7 shows the external surface of the mesh for $\alpha = 12°$. The mesh has $\sim 1.3 \times 10^6$ elements, and $\sim 138 \times 10^6$ degrees of freedom per equation in total when fourth-order solution polynomials are used to represent the solution within each element.

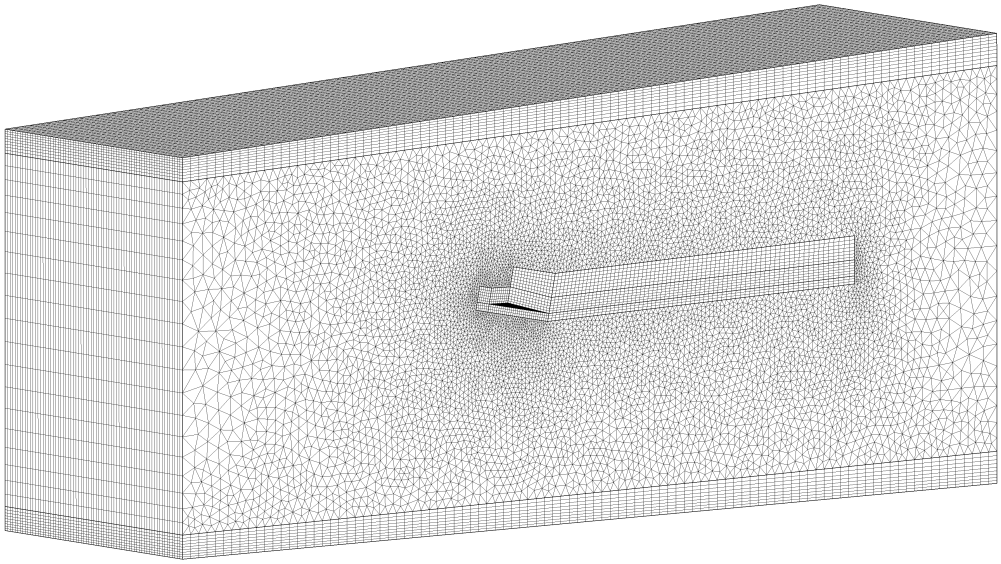


Fig. 7 View of the computational mesh used for the virtual wind tunnel DNS with $\alpha = 12°$.

3. Boundary conditions

At the $x = -15$ inflow a total pressure boundary condition was applied. Specifically, a total pressure $p_T = 34.8804$, a total temperature $T_T = 0.1196$ and an inflow angle normal to the inflow plane were prescribed uniformly. At the $x = 8.333$ outflow plane, a characteristic boundary condition was applied. Specifically, a density $\rho = 1.0$ and a pressure $p = 34.3365$ were prescribed uniformly, along with a spatially varying velocity $\mathbf{v} = \{v_x, v_y, v_z\} = \{(\tanh(8.307(y + 2.803)) - \tanh(8.307(y - 2.803)) - 1.0)(\tanh(8.307z) - \tanh(8.307(z - 3.333)) - 1.0), 0.0, 0.0\}$, which allowed the naturally developing laminar boundary layer within the domain to exit without being perturbed as shown in Fig. 8. An impermeable no-slip adiabatic boundary condition was prescribed at the airfoil surface and the wind tunnel walls. Taken together these conditions achieved $M = 0.15$ and $Re = 3,000$. Note that no boundary layer and no turbulence was injected at the inflow.

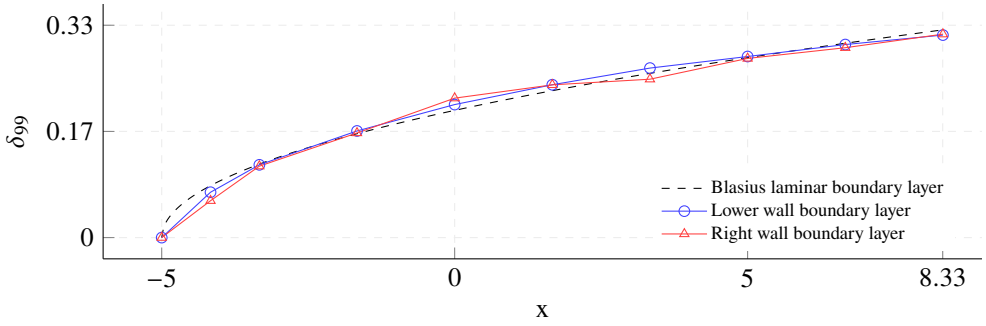


Fig. 8 Plot of the boundary layer thickness δ_{99} as a function of x for the virtual wind tunnel DNS with $\alpha = 11°$ on the lower and right-hand-side walls, measured at the mid-span and mid-height respectively, alongside with the Blasius laminar boundary layer thickness.

4. Startup process and data extraction

All simulations were initiated at $t = 0$ with a uniform density $\rho = 1.0$, velocity $\mathbf{v} = \{v_x, v_y, v_z\} = \{1.0, 0.0, 0.0\}$ and pressure $p = 34.3365$ throughout the entire domain. Simulations were advanced a period t_t to remove initial transients, where $t_t = 96t_c$ when $\alpha < 8$ and $t_t = 144t_c$ when $\alpha \geq 8$, and then a further period t_e, henceforth referred to as the Data Extraction Period during which data was extracted for analysis, where $t_e = 48t_c$ when $\alpha < 8$ and $t_e = 72t_c$ when $\alpha \geq 8$, and with in all cases $t_c = c/u_\infty$ where u_∞ is the x-velocity magnitude measured at the centre of the $x = -5$ inflow plane time-averaged over the Data Extraction Period.

C. Results

Full-span DNS in a virtual wind tunnel captures two important aspects of the flow physics that are not present in the previous span-wise periodic DNS. Specifically, blockage effects are captured, as are interactions between side wall boundary layers and the triangular airfoil, which lead to span-wise variations in the flow field.

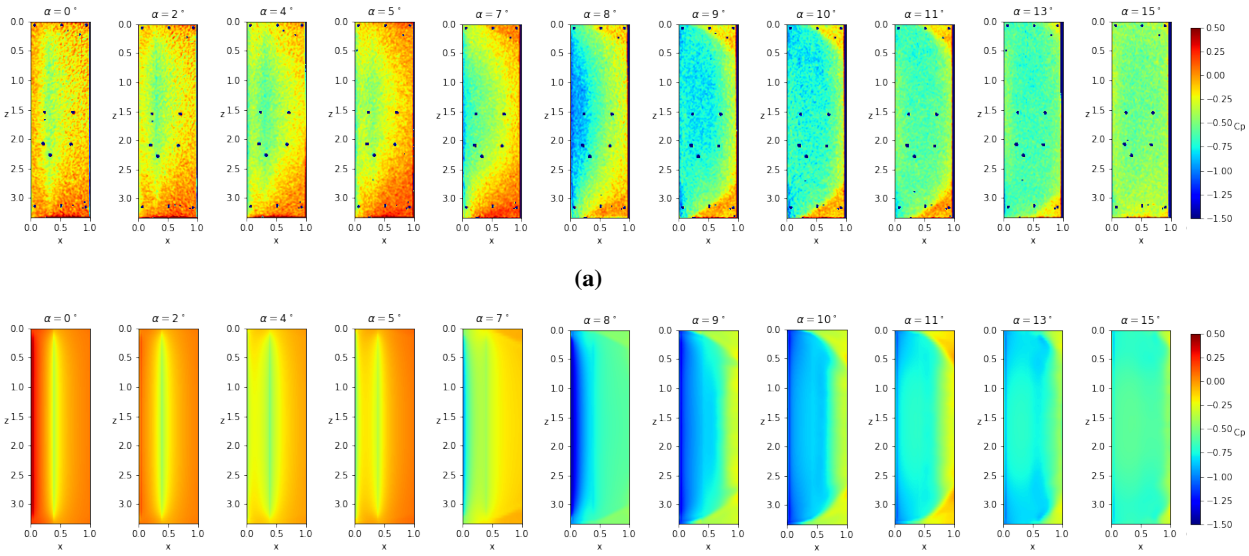
Figure 3 shows plots of C_L and C_D as a function of α for DNS in a virtual wind tunnel undertaken with PyFR, as well as for the previous DNS and experimental studies of Munday et al.[9]. For the PyFR simulations C_L and C_D were obtained using Eq. (1), where F_L and F_D were obtained by time-averaging the sum of viscous and pressure forces on the airfoil in the y and x directions, respectively, over the Data Extraction Period, and q_∞ was obtained via Eq. (9), where ρ_∞ and u_∞ are the density and velocity magnitude, respectively, measured at the centre of the $x = -5$ inflow plane time-averaged over the Data Extraction Period.

Results from DNS in a virtual wind tunnel are seen to be in excellent agreement with the experimental C_L and C_D for low α. This agreement is markedly better than that achieved using span-wise periodic DNS. Moreover, it extends through to $\alpha = 9°$, past the point at which separation migrates from the apex to the leading edge of the airfoil. Indeed, at e.g. $\alpha = 8°$ the resulting error in C_L relative to the experimental data is 95% less than that achieved using span-wise periodic DNS. Finally, we note that when $\alpha > 9°$ discrepancies begin to emerge between results from DNS in a virtual wind tunnel and the experimental C_L and C_D. However, these discrepancies are on the whole less than, or at worst similar to, those achieved using span-wise periodic DNS.

Figure 4 shows plots of C_P for $\alpha = 6°$ and $\alpha = 12°$ on the suction surface of the airfoil as a function of $\tilde{x}$, for DNS in a virtual wind tunnel undertaken with PyFR, as well as for the previous DNS and experimental studies of Munday et al.[9]. For the DNS in a virtual wind tunnel C_P was obtained using Eq. (1), where p was obtained at each $\tilde{x}$ by time-averaging mid-span static pressure on the suction surface of the airfoil over the Data Extraction Period, p_a was obtained by space-time-averaging static pressure within the two mid-span mesh cells that had vertices coincident with the apex of the airfoil and over the Data Extraction Period, and q_∞ was obtained via Eq. (9), where ρ_∞ and u_∞ are the density and velocity magnitude, respectively, measured at the centre of the $x = -5$ inflow plane time-averaged over the Data Extraction Period.

When $\alpha = 6°$ results from DNS in a virtual wind tunnel are seen to be in good agreement with mid-span C_P obtained from the previous DNS and experiments of Munday et al. [9]. However, when $\alpha = 12°$ differences occur. Specifically, DNS in a virtual wind tunnel over-predicts C_P above the down-stream section of the airfoil relative to the experimental results. The discrepancies are similar to those that occur for span-wise periodic DNS with $\delta_z = 0.6$ and $\delta_z = 0.9$.

Figure 9 shows distributions of C_P on the suction surface of the airfoil for DNS in a virtual wind tunnel undertaken with PyFR, as well as for the experimental studies of Munday et al.[9]. For the PyFR simulations C_P distributions were obtained using Eq. (1), where p was obtained by time-averaging static pressure on the suction surface of the airfoil over the Data Extraction Period, plus an additional constant but α dependent shift; calculated to ensure each distribution had the same span-wise average at the apex as the analogous experimental distribution. This shift was applied in order to enable (at least qualitative) comparison between results, under the constraint that precise values of the normalization constants used to obtain the experimental C_P distributions were no longer available. For all α, results from DNS in a virtual wind tunnel are seen to be in good qualitative agreement with C_P distributions obtained experimentally by Munday et al. [9].



(a)

(b)

Fig. 9 Plots of C_P distribution on the suction surface of the wing obtained by experimental studies of Munday et al. [9] (a) and DNS in a virtual wind tunnel using PyFR (b).

Figure 10 shows instantaneous Q-criterion iso-surfaces, coloured by velocity magnitude, for various α, obtained using span-wise periodic DNS with $\delta_z = 0.9$, and DNS in a virtual wind tunnel. It can be seen that even for low α DNS in a virtual wind tunnel leads to breakdown of span-wise uniform coherent structures, and hence 3D flow physics. In contrast, flow remains entirely 2D for span-wise periodic DNS when α is low.

Figure 11 shows time-averaged velocity magnitude distributions in the mid-span plane with superimposed velocity

Line Integral Convolutions (LICs), for various α, obtained using span-wise periodic DNS with $\delta_z = 0.9$, and DNS in a virtual wind tunnel. It can be seen that when $\alpha = 8^\circ$ flow is fully separated from the leading edge for the span-wise periodic DNS. However, this does not occur until $\alpha = 9^\circ$ for DNS in a virtual wind tunnel. Suppression, in this way, of the point at which leading edge separation occurs with α is what leads to the excellent agreement with experimental C_L and C_D through to $\alpha = 9^\circ$ shown in Figure 3.

V. Conclusions

In the present work PyFR was used to undertake high-order GPU-accelerated DNS of flow over a triangular airfoil at a range of angles of attack, with a fixed free-stream Mach number of 0.15 and chord-based Reynolds number of 3,000.

To begin, span-wise periodic DNS of the triangular airfoil were undertaken. It was found that extending the domain span from $\delta_z = 0.3$ to $\delta_z = 0.6$ improved agreement with associated wind tunnel data. However, extending it further to $\delta_z = 0.9$ provided little additional benefit. In particular, on extending δ_z from 0.3 to 0.6 better agreement with C_L, C_D and mid-span C_P distributions were achieved at high angles of attack ($\alpha > 9^\circ$), when the flow is separated. This is because $\delta_z = 0.3$ was found to artificially suppress three-dimensional breakdown of coherent structures that form above the suction surface of the airfoil and in the wake. However, despite this improvement, discrepancies remained between the span-wise periodic DNS results and associated wind tunnel data for all angles of attack studied.

Subsequently, full-span DNS of the triangular airfoil in a wind tunnel were undertaken, including all the wind tunnel walls. These simulations, which attempt to properly capture blockage effects and the interaction of wall boundary layers with the airfoil, led to further improved agreement with associated wind tunnel data. Specifically, better agreement with C_L and C_D was achieved for all angles of attack compared with the span-wise periodic DNS results. In particular, excellent agreement was achieved for low angles of attack ($\alpha < 7^\circ$) and in the region where the separation point transitioned from the apex to the leading edge ($7^\circ < \alpha < 9^\circ$). Moreover, good qualitative agreement was achieved with spatially resolved C_P distributions on the suction surface of the airfoil for all angles of attack studied.

The results are important in terms of understanding discrepancies between previous span-wise periodic DNS of triangular airfoils and associated wind tunnel data. They also demonstrated the utility of high-order GPU-accelerated DNS as a tool for accurately resolving flow physics associated with triangular airfoils under Martian atmospheric conditions.

Future work should investigate how non-sharp leading/trailing edges, inlet turbulence, and wall boundary layer thickness can affect DNS results, with a particular focus on ascertaining whether they account for remaining discrepancies between DNS results and associated wind tunnel data at high angles of attack ($\alpha > 9^\circ$). Future work should also further investigate the unsteady flow physics associated with transition from the apex separation to leading edge separation in the region $7^\circ < \alpha < 9^\circ$, including the effect of wind tunnel walls on this process.

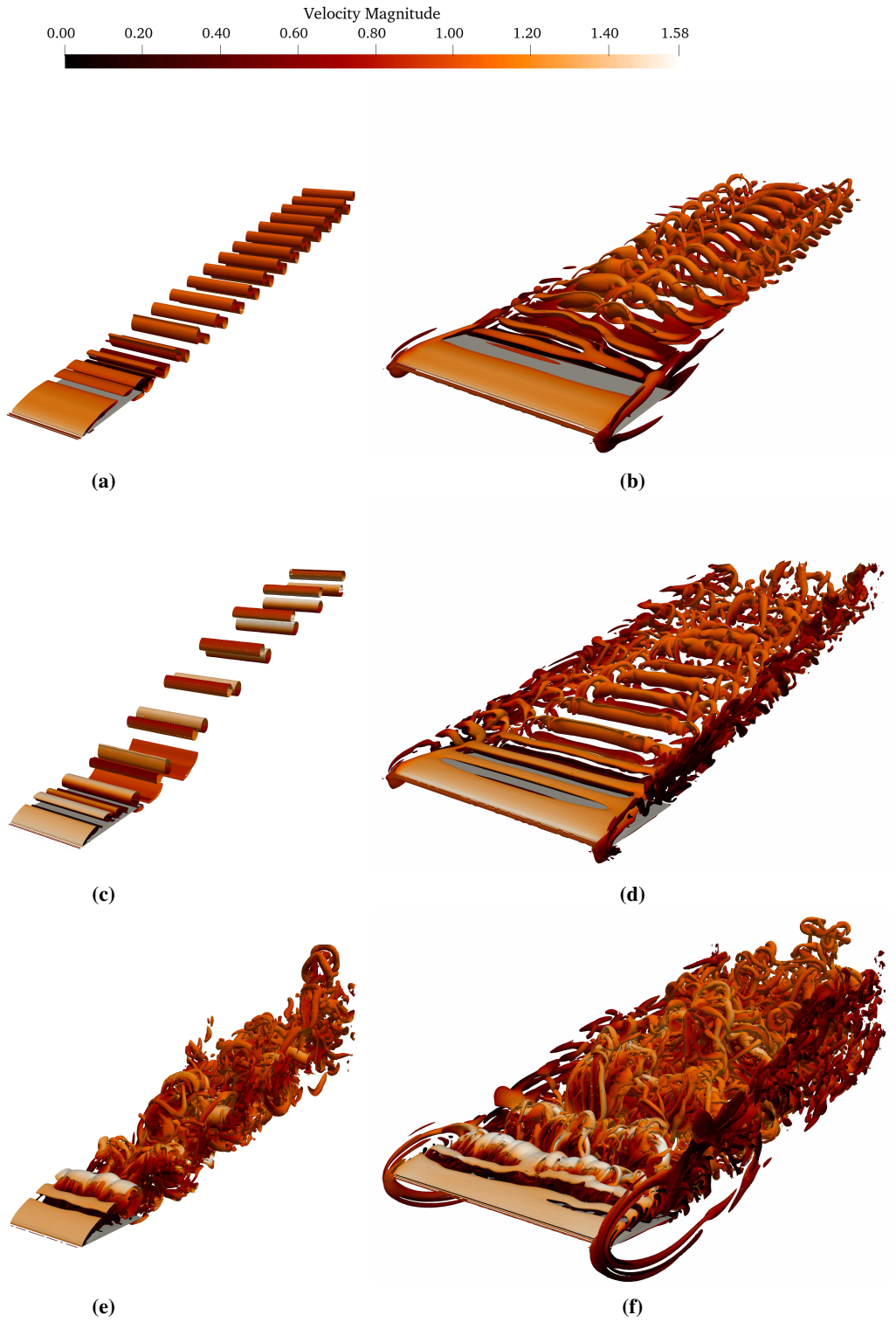


Fig. 10 Images of instantaneous Q-criterion isosurfaces Q = 1, coloured by velocity magnitude, for angles of attack $\alpha = 6^\circ$ (a) and (b), $\alpha = 8^\circ$ (c) and (d), and $\alpha = 15^\circ$ (e) and (f), from span-wise periodic DNS with span $\delta_z = 0.9$ (a), (c) and (e), and virtual wind tunnel DNS (b), (d) and (f).

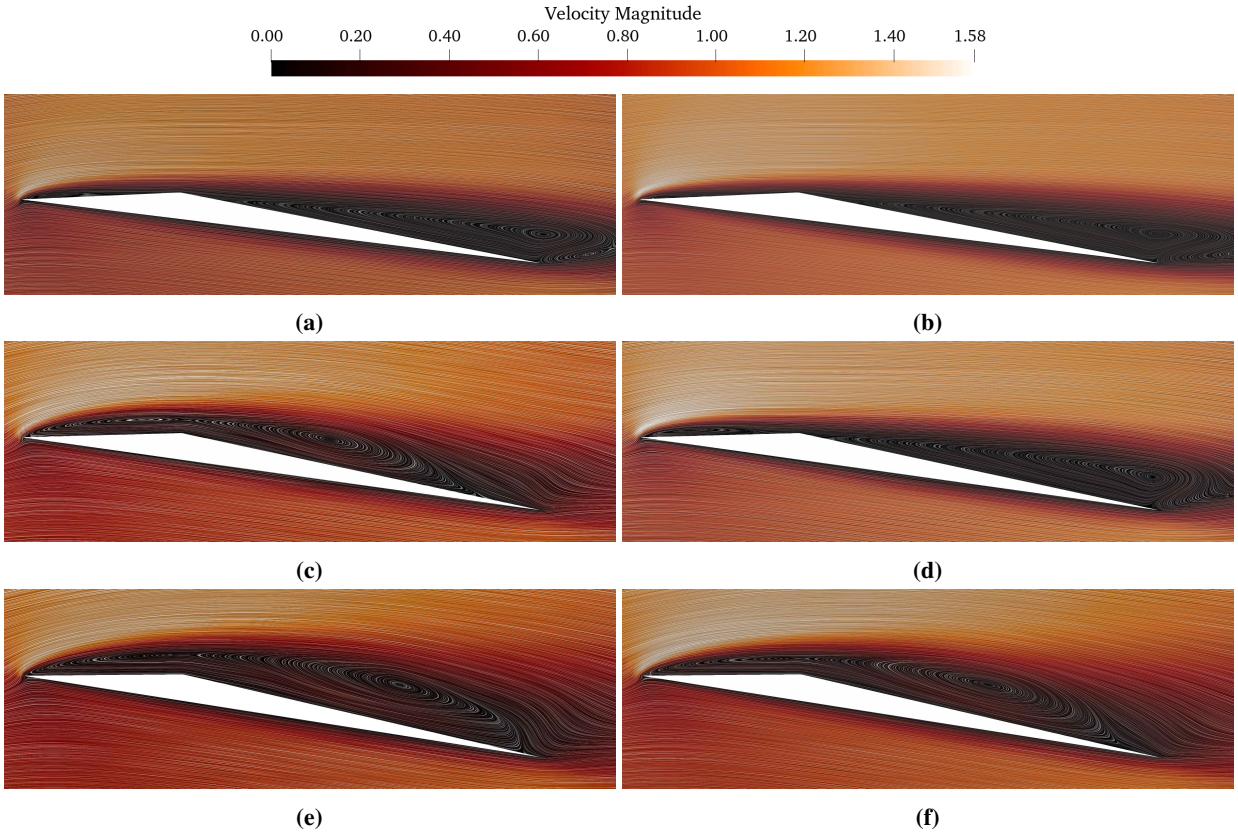


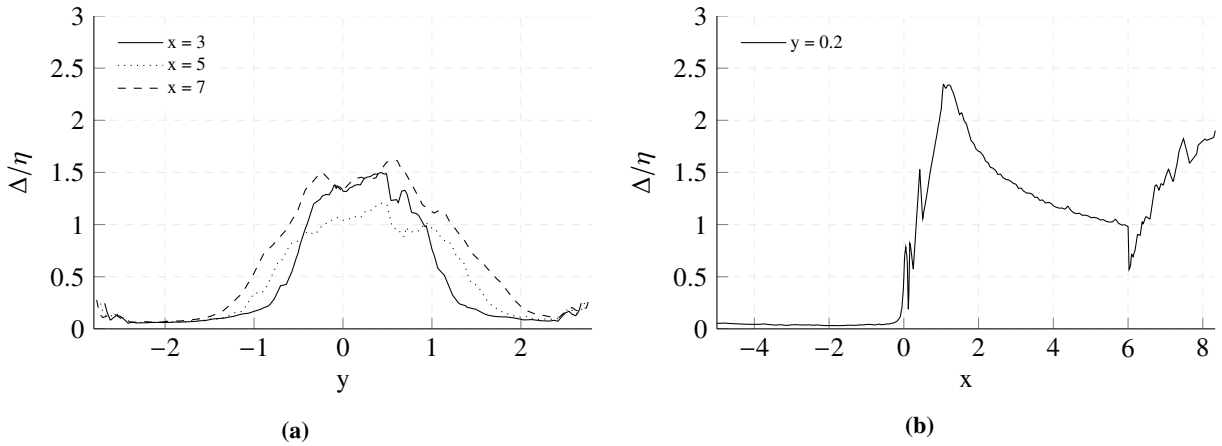
Fig. 11 Images of time-averaged velocity magnitude distributions in the mid-span plane with superimposed velocity Line Integral Convolutions (LICs) for angles of attack $\alpha = 7°$ (a) and (b), $\alpha = 8°$ (c) and (d), and $\alpha = 9°$ (e) and (f), from span-wise periodic DNS with span $\delta_z = 0.9$ (a), (c) and (e), and virtual wind tunnel DNS (b), (d) and (f).

Appendix A

DNS in a virtual wind tunnel with $\alpha = 15°$ was re-started from $t = 144t_c$ and run for a further $383t_c$ during which data was extracted for analysis. Figure 12 shows plots of Δ/η along various mid-span lines within the computational domain, where Δ is an estimate of the solution point spacing given by Eq. (10) and η is an estimate of the Kolmogorov length scale given by Eq. (11). The simulation was undertaken using PyFR v1.12.0.

Acknowledgements

The authors are grateful for support from the Engineering and Physical Sciences Research Council via an EPSRC Fellowship (EP/R030340/1) and for the granted allocations on the High Performance Computing system Cirrus of Edinburgh Parallel Computing Centre (EPCC) and the Piz Daint supercomputer at the Swiss National Supercomputing Centre (CSCS).



(a) **(b)**

Fig. 12 Plots of Δ/η in the mid-span plane as a function of y at x = 3, x = 5 and x = 7 (a) and as a function of x at y = 0.2 (b) for $\alpha = 15°$ from virtual wind tunnel DNS using PyFR.

CRediT authorship contribution statement

L. Caros: Conceptualization, Data Curation, Investigation, Methodology, Visualization, Writing - original draft, Writing - review & editing. **O.R.H. Buxton:** Conceptualization, Supervision, Writing - review & editing. **T. Shigeta:** Data Curation. **T. Nagata:** Data Curation. **T. Nonomura:** Data Curation. **K. Asai:** Data Curation, Supervision. **P.E. Vincent:** Conceptualization, Supervision, Writing - review & editing, Funding Acquisition.

References

[1] Balaram, J. B., Canham, T., Duncan, C., Golombek, M., Grip, H. F., Johnson, W., Maki, J., Quon, A., Stern, R., and Zhu, D., "Mars helicopter technology demonstrator," *AIAA Atmospheric Flight Mechanics Conference*, 2018. https://doi.org/10.2514/6.2018-0023.

[2] Koning, W. J. F., Johnson, W., and Grip, H. F., "Improved Mars Helicopter Aerodynamic Rotor Model for Comprehensive Analyses," *AIAA Journal*, Vol. 57, 2019, pp. 3969–3979.

[3] Anyoji, M., Nonomura, T., Aono, H., Oyama, A., Fujii, K., Nagai, H., and Asai, K., "Computational and experimental analysis of a high-performance airfoil under low-reynolds-number flow condition," *Journal of Aircraft*, Vol. 51, No. 6, 2014, pp. 1864–1872. https://doi.org/10.2514/1.C032553.

[4] Anyoji, M., Nose, K., Ida, S., Numata, D., Nagai, H., and Asai, K., "Low Reynolds Number Airfoil Testing in a Mars Wind Tunnel," *40th Fluid Dynamics Conference and Exhibit*, Chicago, Illinois: 2010. https://doi.org/10.2514/6.2010-4627.

[5] Nagai, H., Asai, K., Numata, D., Suwa, T., and Anyoji, M., "Characteristics of low-Reynolds number airfoils in a mars wind tunnel," *51st AIAA Aerospace Sciences Meeting including the New Horizons Forum and Aerospace Exposition*, 2013.

[6] Obata, A., and Sinohara, S., "Flow Visualization Study of the Aerodynamics of Modeled Dragonfly Wings," *AIAA Journal*, Vol. 47, 2009, pp. 3043–3046. https://doi.org/10.2514/1.43836.

[7] Okamoto, M., and Azuma, A., "Experimental Study on Aerodynamic Characteristics of Unsteady Wings at Low Reynolds Number," *AIAA Journal*, Vol. 43, 2005, pp. 2526–2536.

[8] Hidaka, H., and Okamoto, M., "An Experimental Study of Triangular Airfoils for Mars Airplane," *Transactions of the Japan Society for Aeronautical and Space Sciences, Aerospace Technology Japan*, Vol. 12, 2014, pp. 21–27. https://doi.org/10.2322/tastj.12.Pk_21.

[9] Munday, P., Taira, K., Suwa, T., Numata, D., and Asai, K., "Non-linear Lift on a Triangular Airfoil in Low-Reynolds-Number Compressible Flow," *Journal of Aircraft*, Vol. 52, 2015, pp. 924–931. https://doi.org/10.2514/1.C032983.

[10] Suwa, T., Nose, K., Numata, D., Nagai, H., and Asai, K., "Compressibility Effects on Airfoil Aerodynamics at Low Reynolds Number," *30th AIAA Applied Aerodynamics Conference*, New Orleans, Louisiana: 2012. https://doi.org/10.2514/6.2012-3029.

[11] Yang, H., and Agarwal, R., "CFD Simulations of a Triangular Airfoil for Martian Atmosphere in Low-Reynolds Number Compressible Flow," 2019. https://doi.org/10.2514/6.2019-2923.

[12] Han, X., Rahman, M., and Agarwal, R., "Wall-Distance Free Wray-Agarwal Turbulence Model with Elliptic Blending," AIAA Aviation Forum, Denver, 2018. https://doi.org/10.2514/6.2018-4044.

[13] Witherden, F., Farrington, A., and Vincent, P., "PyFR: An Open Source Framework for Solving Advection-Diffusion Type Problems on Streaming Architectures using the Flux Reconstruction Approach," *Computer Physics Communications*, Vol. 185, 2014, pp. 3028–3040. https://doi.org/10.1016/j.cpc.2014.07.011.

[14] Anyoji, M., Nose, K., Ida, S., Numata, D., Nagai, H., and Asai, K., "Development of a Low-Density Wind Tunnel for Simulating Martian Atmospheric Flight," *Transactions of the Japanese Society for Artificial Intelligence, Aerospace Technology Japan*, Vol. 9, 2011, p. 21–27. https://doi.org/10.2322/tastj.9.21.

[15] Huynh, H., "A Flux Reconstruction Approach to High-Order Schemes Including Discontinuous Galerkin Methods," *AIAA Paper 4079*, 2007, pp. 1–42.

[16] Kennedy, C. A., Carpenter, M. H., and Lewis, R., "Low-storage, explicit Runge–Kutta schemes for the compressible Navier–Stokes equations," *Applied Numerical Mathematics*, Vol. 35, No. 3, 2000, pp. 177–219. https://doi.org/https://doi.org/10.1016/S0168-9274(99)00141-5, URL https://www.sciencedirect.com/science/article/pii/S0168927499001415.

[17] Buxton, O., Laizet, S., and Ganapathisubramani, B., "The effects of resolution and noise on kinematic features of fine-scale turbulence," *Experiments in Fluids*, Vol. 51, No. 5, 2011, pp. 1417–1437. https://doi.org/10.1007/s00348-011-1159-2.